PHYSICAL REVIEW B VOLUME 50, NUMBER 19 15 NOVEMBER 1994-I

# Theory of magnetotransport in a composite medium with periodic microstructure for arbitrary magnetic fields

Yakov M. Strelniker and David J. Bergman
*School of Physics and Astronomy, Raymond and Beverly Sackler Faculty of Exact Sciences,*
*Tel Aviv University, Tel Aviv 69978, Israel*
(Received 27 May 1994)

A method is described for calculating the magnetotransport properties of a two-component composite conducting medium which has a periodic microstructure. The method is based on a Fourier series expansion of the local electric potential. Because a large number of expansion coefficients needs to be used in order to get reliable results for the bulk effective behavior, a special approach is developed that does not require solving a large set of coupled linear algebraic equations for them. Results are presented for the magnetoresistance and Hall resistance as functions of the magnetic field in a number of models where periodic arrays of insulating inclusions of various shapes are embedded in a uniform host material. These samples include cases where the inclusions are well separated as well as cases where they touch and where they overlap.

## I. INTRODUCTION

Composite media are usually either disordered on the microscale, as in the case of granular or polycrystalline materials, or partially ordered, as in the case of fiber reinforced materials. It is only quite recently that highly ordered periodic dielectric composites have been fabricated in the context of a search for materials where a photonic band gap might be observed.[1] In the expectation that conducting composites will also soon be available, fabricated either by the same techniques that were used in Ref. 1 or by photolithography, we initiated a study of magnetotransport in such a medium, with special emphasis on the case where the magnetic field $H$ is strong enough so that the Hall resistivity is large compared to the Ohmic resistivity at least in one of the components. We found and reported earlier that, even if none of the components exhibited any magnetoresistance by itself, the composite invariably had a strong magnetoresistance. Moreover, the Ohmic components of the bulk effective resistivity tensor were found to exhibit a strong dependence on the direction of $H$, which was quite remarkable in its similarity to the angular variations of magnetoresistance in some metallic single crystals.[2] In this article we describe in detail the approach that was developed to attack this problem, and also describe results for the magnetoresistance and Hall resistance of periodic arrays of nonoverlapping as well as overlapping insulating inclusions of various shapes (see Fig. 1) which are embedded in a free-electron conducting host medium. We obtain these results for different values of the magnetic field which range all the way from very weak to very strong.

Magnetotransport in a composite conductor was discussed in the past mainly in the context of weak fields $H$.[3–13] In that case, when the Hall resistivity $\rho_H$ is much less than the Ohmic resistivity $\rho$ in all components, the focus was mostly on a calculation of the bulk effective Hall resistivity or Hall conductivity. Interesting results were obtained for the behavior of that quantity near a percolation threshold, first in calculations[5,6,8,9,14] and later in experiments.[15,16]

Strong-field magnetotransport in composite media turned out to be a difficult problem, except in the two-dimensional case where the duality transformation leads to some useful exact results which are valid for arbitrary field strengths.[17] In particular, it follows from that transformation that the relative magnetoresistance of a metal-insulator composite is the *same* as that of the pure metal (see also Refs. 18 and 19). In the past

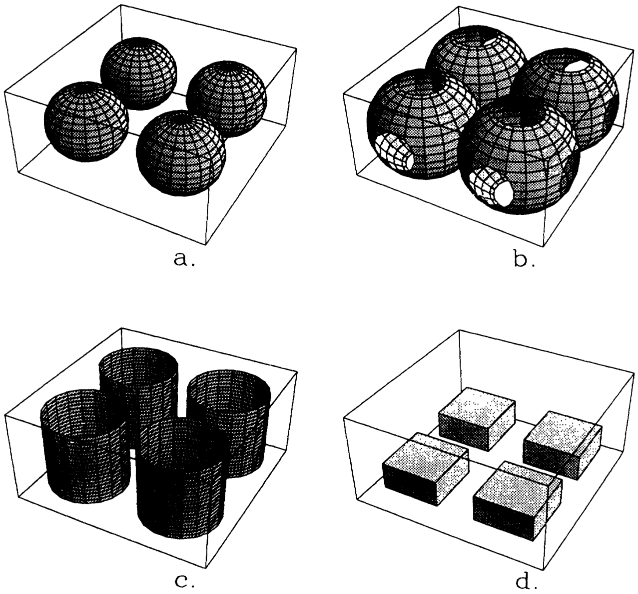

FIG. 1. Possible examples of a periodic composite microstructure with various shapes of inclusions: (a) Nonoverlapping spheres, (b) overlapping spheres, (c) nonoverlapping cylinders, (d) nonoverlapping rectangular prisms.

©1994 The American Physical Society

the only discussions of strong-field magnetotransport in three-dimensional composites were based either on low density or effective medium approximations,[20–23] or involved special microstructures.[10,12,20,24–26] It is only quite recently that accurate calculations have been performed on a regular fractal structure and a random percolating system using a discrete network model.[27,28]

Our approach to magnetotransport in a periodic composite medium is based on the fact that the local electric potential $\phi(\mathbf{r})$ has a periodic component with the same periodicity as the underlying microstructure. Consequently, it can be expanded in an appropriate Fourier series, and the differential equation for $\phi(\mathbf{r})$ is then transformed into an infinite set of linear algebraic equations for the expansion coefficients. What makes this approach nontrivial is that we have succeeded in taking into account a far greater number of these coefficients than one could hope to obtain by a straightforward solution of those equations.

The rest of this article is organized as follows. In Sec. II we describe in some detail the approach that we developed for calculating the magnetotransport properties of a periodic conducting composite. In Sec. III we describe some technical aspects of the computations and present the results for a number of systems with different types of insulating inclusions. Section IV provides a discussion of those results and some of their implications. In Appendix A we discuss the analytic properties of a function that plays a crucial role in the theory, and how we attempted to evaluate it from a divergent power series expansion. In Appendix B we derive closed form expressions for the Fourier coefficients of the characteristic or indicator functions that characterize some of the microstructures that were studied, and a series expansion for these coefficients in the case of an overlapping spheres microstructure.

## II. THEORY

### A. Magnetotransport in a composite medium

In the presence of a magnetic field, the conductivity as well as the resistivity become nonsymmetric tensors which must be represented by matrices. In a composite medium these tensors usually have a different value in each component. In the case of a two-component composite we use the characteristic or indicator function of component No. 1, defined by

$$\theta_1(\mathbf{r}) = \begin{cases} 1 & \text{for } \mathbf{r} \text{ inside component No. 1,} \\ 0 & \text{otherwise,} \end{cases} \tag{2.1}$$

in order to represent the position dependent conductivity tensor $\hat{\sigma}(\mathbf{r})$ as

$$\hat{\sigma}(\mathbf{r}) = \hat{\sigma}_1\theta_1 + \hat{\sigma}_2(1-\theta_1) = \hat{\sigma}_2 - \delta\hat{\sigma}\theta_1, \tag{2.2}$$

$$\delta\hat{\sigma} \equiv \hat{\sigma}_2 - \hat{\sigma}_1, \tag{2.3}$$

where $\hat{\sigma}_1$, $\hat{\sigma}_2$ are the conductivity tensors of the two components.

The bulk effective conductivity tensor of the composite $\hat{\sigma}_e$ is defined as providing the linear relationship between the volume averages of the electric field $\nabla\phi(\mathbf{r})$ and the current density $\mathbf{J}(\mathbf{r}) \equiv \hat{\sigma}(\mathbf{r})\nabla\phi(\mathbf{r})$

$$\langle \mathbf{J} \rangle \equiv \hat{\sigma}_e \langle \nabla\phi(\mathbf{r}) \rangle. \tag{2.4}$$

The final result for $\hat{\sigma}_e$ will be independent of the precise way in which the local electric potential is created, provided that the composite microstructure, as well as the boundary conditions that determine $\phi(\mathbf{r})$, are macroscopically homogeneous. We are, therefore, free to choose the most convenient among a rather general class of possible boundary conditions when setting up a scheme for calculating $\phi(\mathbf{r})$.

We choose a scheme where the composite medium occupies the entire volume in between the infinitely conducting plates of a parallel plate capacitor (see Fig. 2). The plates are taken to be infinitely large, and the distance between them is taken to be finite but large compared to any scale of inhomogeneity of the system. Keeping the medium and the magnetic field fixed, we can choose the orientation of the plates to be perpendicular to any of the coordinate axes. We denote by $\phi^{(\alpha)}(\mathbf{r})$ the local potential field that results when the plates are perpendicular to the $r_\alpha$ axis and a potential difference equal to their distance apart $L$ is applied between them. The volume averaged electric field is then $\langle \nabla\phi^{(\alpha)} \rangle = \nabla r_\alpha = \mathbf{e}_\alpha$, i.e., a unit vector in the $r_\alpha$ direction.

The potential field $\phi^{(\alpha)}(\mathbf{r})$ is usually taken to be determined as the solution of a boundary value problem with a partial differential equation that follows from the current conservation condition $\nabla \cdot \mathbf{J}(\mathbf{r}) = 0$, namely

$$\nabla \cdot \hat{\sigma}(\mathbf{r}) \cdot \nabla\phi^{(\alpha)}(\mathbf{r}) = 0 \quad \text{inside the capacitor,} \tag{2.5}$$

$$\phi^{(\alpha)}(\mathbf{r}) = 0, L \quad \text{for } r_\alpha = 0, L, \quad \text{i.e., at the capacitor plates.} \tag{2.6}$$

We find it more convenient to base our discussion on an integral equation for $\phi^{(\alpha)}(\mathbf{r})$.

In order to obtain such an equation, we first use (2.2) to rewrite (2.5) as

$$\nabla \cdot \hat{\sigma}_2 \cdot \nabla\phi^{(\alpha)} = \nabla \cdot \theta_1\delta\hat{\sigma} \cdot \nabla\phi^{(\alpha)}. \tag{2.7}$$

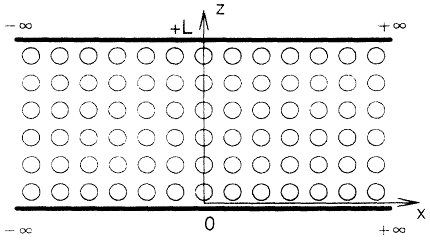

FIG. 2. Scheme used to set up the calculation of the electrical potential $\phi(\mathbf{r})$ in a two-component conducting composite. The direction of $\mathbf{H}$ is arbitrary. The average electric field $\langle \mathbf{E} \rangle = \mathbf{E}_0$ lies along the $z$ axis, which is perpendicular to the two equipotential plates.

We then define a Green function $G(\mathbf{r},\mathbf{r}'|\hat{\sigma}_2)$ as the solution of the following boundary value problem:

$$\nabla\cdot\hat{\sigma}_2\cdot\nabla G=-\delta^3(\mathbf{r}-\mathbf{r}')\ \text{ inside the capacitor,} \tag{2.8}$$

$$G=0\ \text{ at the capacitor plates,} \tag{2.9}$$

and use it to "solve" (2.7) and (2.6) by treating the right-hand side of (2.7) as though it were given. In this way we obtain

$$\begin{aligned}\phi^{(\alpha)}(\mathbf{r})&=r_\alpha-\int dV'G(\mathbf{r},\mathbf{r}'|\hat{\sigma}_2)\nabla'\cdot\theta_1(\mathbf{r}')\delta\hat{\sigma}\cdot\nabla'\phi^{(\alpha)}(\mathbf{r}')\\&=r_\alpha+\int dV'\theta_1(\mathbf{r}')\nabla'G(\mathbf{r},\mathbf{r}'|\hat{\sigma}_2)\cdot\delta\hat{\sigma}\cdot\nabla'\phi^{(\alpha)}(\mathbf{r}')\\&=r_\alpha+\hat{\Gamma}\phi^{(\alpha)},\end{aligned} \tag{2.10}$$

where we used integration by parts to get the second line and where the linear integro-differential operator $\hat{\Gamma}$ is defined by

$$\hat{\Gamma}\phi\equiv\int dV'\theta_1(\mathbf{r}')\nabla'G(\mathbf{r},\mathbf{r}'|\hat{\sigma}_2)\cdot\delta\hat{\sigma}\cdot\nabla'\phi(\mathbf{r}'). \tag{2.11}$$

Although $G$, and hence also $\hat{\Gamma}$, depend on the orientation of the capacitor plates, this dependence is only important if at least one of $\mathbf{r}$, $\mathbf{r}'$ is near the plates. For most purposes $G$ can be approximated by the Green function that vanishes at infinity, and in that case the only dependence of (2.10) on the boundary conditions comes from the term $r_\alpha$, which ensures that $\phi^{(\alpha)}$ satisfies them. The microstructure enters into $\hat{\Gamma}$ through the characteristic function $\theta_1(\mathbf{r})$. Due to the symmetric dot products of $\hat{\sigma}_2$ and the two $\nabla$ operators in (2.8), the antisymmetric part of $\hat{\sigma}_2$ does not participate in that equation. Therefore, $G(\mathbf{r},\mathbf{r}'|\hat{\sigma}_2)$ actually only depends on the symmetric part $\hat{\sigma}_{2s}$ of $\hat{\sigma}_2$. The Green function that vanishes at infinity depends on $\mathbf{r}$, $\mathbf{r}'$ only through their difference $\mathbf{r}-\mathbf{r}'$. In the case where $\hat{\sigma}_{2s}$ is a diagonal tensor, this Green function has a relatively simple closed form, namely[22]

$$\frac{1}{4\pi\left(\sigma^{(2)}_{xx}\sigma^{(2)}_{yy}\sigma^{(2)}_{zz}\right)^{1/2}}\left(\frac{(x-x')^2}{\sigma^{(2)}_{xx}}+\frac{(y-y')^2}{\sigma^{(2)}_{yy}}+\frac{(z-z')^2}{\sigma^{(2)}_{zz}}\right)^{-1/2}. \tag{2.12}$$

The Fourier transform of the $G$ which vanishes at infinity has an even simpler form, namely

$$\int dVe^{-i\mathbf{k}\cdot(\mathbf{r}-\mathbf{r}')}G(\mathbf{r},\mathbf{r}'|\hat{\sigma}_{2s})=\frac{1}{\mathbf{k}\cdot\hat{\sigma}_{2s}\cdot\mathbf{k}}, \tag{2.13}$$

which is valid regardless of the detailed form of $\hat{\sigma}_{2s}$. This result is easily obtained by performing a Fourier transformation of (2.8).

The distorted part of $\phi^{(\alpha)}(\mathbf{r})$ is defined by

$$\psi^{(\alpha)}(\mathbf{r})\equiv\phi^{(\alpha)}(\mathbf{r})-r_\alpha, \tag{2.14}$$

and satisfies an integral equation which immediately follows from (2.10)

$$\psi^{(\alpha)}=\hat{\Gamma}r_\alpha+\hat{\Gamma}\psi^{(\alpha)}. \tag{2.15}$$

This equation can be solved symbolically by using the resolvent operator $1/(1-\hat{\Gamma})$

$$\psi^{(\alpha)}(\mathbf{r})=\frac{\hat{\Gamma}}{1-\hat{\Gamma}}r_\alpha. \tag{2.16}$$

While it is usually impossible to calculate the resolvent operator in closed form, we shall see in the following subsection that it can sometimes be useful to express it as a power series in $\hat{\Gamma}$ or $\delta\hat{\sigma}$.

Using (2.4) and (2.2) we can write for $\hat{\sigma}_e$

$$\hat{\sigma}_e\cdot\langle\nabla\phi^{(\alpha)}\rangle=\hat{\sigma}_2\cdot\langle\nabla\phi^{(\alpha)}\rangle-\delta\hat{\sigma}\cdot\langle\theta_1\nabla\phi^{(\alpha)}\rangle. \tag{2.17}$$

This expression can be further processed by using (2.14) and recalling that $\langle\nabla\phi^{(\alpha)}\rangle=\mathbf{e}_\alpha$. In this way we get

$$(\hat{\sigma}_2-\hat{\sigma}_e)\cdot\mathbf{e}_\alpha=\delta\hat{\sigma}\cdot\langle\theta_1\nabla r_\alpha\rangle+\delta\hat{\sigma}\cdot\langle\theta_1\nabla\psi^{(\alpha)}\rangle, \tag{2.18}$$

which reduces to

$$(\hat{\sigma}_2-p_1\delta\hat{\sigma}-\hat{\sigma}_e)_{\alpha\beta}=\delta\hat{\sigma}_{\alpha\gamma}\langle\theta_1\nabla_\gamma\psi^{(\beta)}\rangle, \tag{2.19}$$

where $p_1=\langle\theta_1\rangle$ is the volume fraction of the No. 1 component. Here and in the rest of this article we use the convention that a summation over repeated tensor indices is always implied.

### B. Periodic composites

When the composite medium has a periodic microstructure, great simplifications ensue due to the fact that $\theta_1(\mathbf{r})$ is now a periodic function. From the fact that, away from the external boundaries, $G$ depends on $\mathbf{r}$, $\mathbf{r}'$ only through their difference $\mathbf{r}-\mathbf{r}'$ [see (2.12)], we get that for any periodic or linear function $f(\mathbf{r})$, $\hat{\Gamma}f$ is also periodic except near those boundaries. Hence $\psi^{(\alpha)}(\mathbf{r})$ is periodic and can be expanded in a Fourier series

$$\psi^{(\alpha)}(\mathbf{r})=\sum_{\mathbf{g}}\psi^{(\alpha)}_{\mathbf{g}}e^{i\mathbf{g}\cdot\mathbf{r}}, \tag{2.20}$$

where the sum is over all the vectors $\mathbf{g}$ of the appropriate reciprocal lattice. The Fourier expansion coefficient of an arbitrary periodic function $f(\mathbf{r})$ is given by

$$f_{\mathbf{g}}=\frac{1}{V_a}\int_{V_a}dVe^{-i\mathbf{g}\cdot\mathbf{r}}f(\mathbf{r}). \tag{2.21}$$

Instead of the Fourier coefficients $f_{\mathbf{g}}$, it is convenient to introduce the following coefficients:

$$i(\mathbf{g}\cdot\hat{\sigma}_2\cdot\mathbf{g})^{1/2}f_{\mathbf{g}}=i(\mathbf{g}\cdot\hat{\sigma}_{2s}\cdot\mathbf{g})^{1/2}f_{\mathbf{g}}\quad\text{for}\quad\mathbf{g}\neq0. \tag{2.22}$$

These characterize the function $f(\mathbf{r})$ up to an additive constant.

Some straightforward calculations lead to the following results for the Fourier coefficients of $\hat{\Gamma}r_\alpha$ and $\hat{\Gamma}f$, where $f(\mathbf{r})$ is an arbitrary periodic function:

$$i(\mathbf{g}\cdot\hat{\sigma}_{2s}\cdot\mathbf{g})^{1/2}(\hat{\Gamma}r_{\alpha})_{\mathbf{g}} = \frac{g_{\beta}\delta\sigma_{\beta\alpha}\theta_{\mathbf{g}}}{(\mathbf{g}\cdot\hat{\sigma}_{2s}\cdot\mathbf{g})^{1/2}}, \tag{2.23}$$

$$i(\mathbf{g}\cdot\hat{\sigma}_{2s}\cdot\mathbf{g})^{1/2}(\hat{\Gamma}f)_{\mathbf{g}} = \sum_{\mathbf{g}'\neq 0}\Gamma_{\mathbf{g}\mathbf{g}'}\,i(\mathbf{g}'\cdot\hat{\sigma}_{2s}\cdot\mathbf{g}')^{1/2}f_{\mathbf{g}'}, \tag{2.24}$$

$$\Gamma_{\mathbf{g}\mathbf{g}'} \equiv \frac{(\mathbf{g}\cdot\delta\hat{\sigma}\cdot\mathbf{g}')}{(\mathbf{g}\cdot\hat{\sigma}_{2s}\cdot\mathbf{g})^{1/2}(\mathbf{g}'\cdot\hat{\sigma}_{2s}\cdot\mathbf{g}')^{1/2}}\theta_{\mathbf{g}-\mathbf{g}'}, \tag{2.25}$$

where $\theta_{\mathbf{g}}$ is the Fourier coefficient of $\theta_1(\mathbf{r})$. Clearly, the matrix defined in (2.25) represents the integro-differential operator $\hat{\Gamma}$ in this scheme.

We now translate the integro-differential equation (2.15) for $\psi^{(\alpha)}(\mathbf{r})$ into an infinite set of linear algebraic equations for the Fourier coefficients $\psi_{\mathbf{g}}^{(\alpha)}$, which are represented by

$$a_{\mathbf{g}}^{(\alpha)} \equiv i(\mathbf{g}\cdot\hat{\sigma}_{2s}\cdot\mathbf{g})^{1/2}\psi_{\mathbf{g}}^{(\alpha)} \quad \text{for} \quad \mathbf{g}\neq 0. \tag{2.26}$$

This is done by Fourier transforming (2.15) and using (2.23) and (2.24), and leads to

$$a_{\mathbf{g}}^{(\alpha)} = r_{\mathbf{g}}^{(\alpha)} + \sum_{\mathbf{g}'\neq 0}\Gamma_{\mathbf{g}\mathbf{g}'}a_{\mathbf{g}'}^{(\alpha)} \quad \text{for} \quad \mathbf{g}\neq 0, \tag{2.27}$$

$$r_{\mathbf{g}}^{(\alpha)} \equiv \frac{g_{\beta}\delta\sigma_{\beta\alpha}}{(\mathbf{g}\cdot\hat{\sigma}_{2s}\cdot\mathbf{g})^{1/2}}\theta_{\mathbf{g}}, \tag{2.28}$$

which can be solved symbolically by

$$a_{\mathbf{g}}^{(\alpha)} = \sum_{\mathbf{g}'\neq 0}\left(\frac{1}{1-\hat{\Gamma}}\right)_{\mathbf{g}\mathbf{g}'} r_{\mathbf{g}'}^{(\alpha)}. \tag{2.29}$$

Substituting the Fourier expansion of $\psi^{(\alpha)}(\mathbf{r})$ in (2.19), we now get

$$\begin{aligned}(\hat{\sigma}_2 - p_1\delta\hat{\sigma} - \hat{\sigma}_e)_{\alpha\beta} &= \frac{\delta\sigma_{\alpha\gamma}}{V_a}\int_{V_a} dV\theta_1(\mathbf{r})\sum_{\mathbf{g}} ig_{\gamma}\psi_{\mathbf{g}}^{(\beta)}e^{i\mathbf{g}\cdot\mathbf{r}} \\ &= \delta\sigma_{\alpha\gamma}\sum_{\mathbf{g}} ig_{\gamma}\psi_{\mathbf{g}}^{(\beta)}\theta_{-\mathbf{g}} \\ &= \sum_{\mathbf{g}\neq 0}\frac{\delta\sigma_{\alpha\beta}g_{\beta}}{(\mathbf{g}\cdot\hat{\sigma}_{2s}\cdot\mathbf{g})^{1/2}}\theta_{-\mathbf{g}}a_{\mathbf{g}}^{(\beta)}. \end{aligned} \tag{2.30}$$

Note that the coefficient multiplying $a_{\mathbf{g}}^{(\beta)}$ in the last sum looks similar to $r_{\mathbf{g}}^{(\alpha)*}$, but actually differs from it, because $\delta\sigma_{\alpha\beta}\neq\delta\sigma_{\beta\alpha}$.

One way to proceed is to solve (2.27) numerically for the $a_{\mathbf{g}}^{(\alpha)}$, using a truncated version of the $\Gamma_{\mathbf{g}\mathbf{g}'}$ matrix of (2.25), and then use those coefficients in (2.30) in order to evaluate $\hat{\sigma}_e$. Since the $\hat{\Gamma}$ matrix is not sparse, we cannot include too many values of $\mathbf{g}$ in such a calculation. For example, in the case of a simple cubic system with a unit cell of linear size $a$, $\mathbf{g} = \frac{2\pi}{a}(n_x, n_y, n_z)$ with $n_x, n_y, n_z$ as arbitrary integers. If we let each of these integers range from $-5$ to $+5$, then the total number of nonzero $\mathbf{g}$ values is $11^3 - 1 = 1330$, resulting in a $\hat{\Gamma}$ matrix of size $1330 \times 1330$. This is about the largest size that can be conveniently used in solving (2.27) on a modern workstation. From experience with a related problem (see Ref. 29), we expect that greater values of $\mathbf{g}$ are needed in order to obtain accurate results for $\hat{\sigma}_e$ in the case of a nondilute composite.

In order to include more values of $\mathbf{g}$ in the calculation, we use a different approach, similar to the one first used in Ref. 29. The basic idea is to substitute the symbolic solution (2.29), written in a slightly different form, namely

$$a_{\mathbf{g}}^{(\alpha)} = \sum_{\mathbf{g}'\neq 0}\left(\frac{1}{s-\hat{\Gamma}}\right)_{\mathbf{g}\mathbf{g}'} r_{\mathbf{g}'}^{(\alpha)}\Bigg|_{s=1}, \tag{2.31}$$

in (2.30), and then expand the result in powers of $1/s$. This leads to

$$(\hat{\sigma}_2 - p_1\delta\hat{\sigma} - \hat{\sigma}_e)_{\alpha\beta} = F_{\alpha\beta}(1), \tag{2.32}$$

where

$$\begin{aligned}F_{\alpha\beta}(s) &= \sum_{\mathbf{g}\neq 0}\sum_{\mathbf{g}'\neq 0}\frac{\delta\sigma_{\alpha\beta}g_{\beta}}{(\mathbf{g}\cdot\hat{\sigma}_{2s}\cdot\mathbf{g})^{1/2}}\theta_{-\mathbf{g}}\left(\frac{1}{s-\hat{\Gamma}}\right)_{\mathbf{g}\mathbf{g}'} r_{\mathbf{g}'}^{(\beta)} \\ &= \sum_{r=0}^{\infty}\frac{A_{\gamma\omega}^{(r)}}{s^{r+1}}\delta\sigma_{\alpha\gamma}\delta\sigma_{\omega\beta} \end{aligned} \tag{2.33}$$

$$\begin{aligned}A_{\gamma\omega}^{(r)} \equiv \sum_{\mathbf{g}\neq 0}\sum_{\mathbf{g}'\neq 0}&\frac{g_{\gamma}\theta_{-\mathbf{g}}}{(\mathbf{g}\cdot\hat{\sigma}_{2s}\cdot\mathbf{g})^{1/2}}\left(\hat{\Gamma}^{r}\right)_{\mathbf{g}\mathbf{g}'} \\ &\times\frac{g'_{\omega}\theta_{\mathbf{g}'}}{(\mathbf{g}'\cdot\hat{\sigma}_{2s}\cdot\mathbf{g}')^{1/2}}. \end{aligned} \tag{2.34}$$

The $3\times 3$ matrix of coefficients $A_{\alpha\beta}^{(0)}$ is symmetric, although $A_{\alpha\beta}^{(r)}$ for general $r$ is not, and obeys a certain sum rule

$$A_{\alpha\beta}^{(0)} = \sum_{\mathbf{g}\neq 0}\frac{g_{\alpha}g_{\beta}}{\mathbf{g}\cdot\hat{\sigma}_{2s}\cdot\mathbf{g}}|\theta_{\mathbf{g}}|^2 = A_{\beta\alpha}^{(0)} \tag{2.35}$$

$$\begin{aligned}\mathrm{Tr}(\hat{A}^{(0)}\hat{\sigma}_{2s}) &= \sum_{\mathbf{g}\neq 0}|\theta_{\mathbf{g}}|^2 = \sum_{\text{all }\mathbf{g}}|\theta_{\mathbf{g}}|^2 - \theta_0^2 \\ &= \frac{1}{V_a}\int_{V_a} dV\theta_1^2 - \left(\frac{1}{V_a}\int_{V_a} dV\theta_1\right)^2 \\ &= p_1 - p_1^2 = p_1(1-p_1), \end{aligned} \tag{2.36}$$

which is used to test the accuracy of numerical computations with truncated sets of $\mathbf{g}$ vectors.

In calculating the expansion coefficients $A_{\alpha\beta}^{(r)}$, we do not need to keep in memory the entire matrix $\Gamma_{\mathbf{g}\mathbf{g}'}$: when we apply this matrix to any column vector, we only need to use it one row at a time, and each row can be re-constructed every time it is needed by using (2.25). All that we need to store are the Fourier expansion coefficients $\theta_{\mathbf{g}}$ of $\theta_1(\mathbf{r})$. Consequently, we do not run into any memory limitations, such as would be the case if we tried to solve the set of equations (2.27), which would require keeping the entire $\hat{\Gamma}$ matrix in memory. Furthermore, if $\Gamma_{\mathbf{gg}'}$ is an $n \times n$ matrix, then the number of basic arithmetic operations needed to calculate $A^{(r)}_{\alpha\beta}$ is of order $O(rn^2)$, compared to $O(n^3)$ operations which are needed to solve (2.27). Thus, for $r \ll n$ a huge reduction in computing time is achieved. In fact, working with a Sun Sparcl workstation we have been able to use $\mathbf{g}$ vectors with integer components ranging from $-10$ to $+10$ in all directions, a total of $21^3 - 1 = 9260$ different $\mathbf{g}$ vectors. The only limitation was due to computing time and not memory requirements, so this number could easily be increased by a factor of 10 (i.e., $\mathbf{g}$ vectors with integer components ranging from $-15$ to $+15$ in all directions) just by using a faster workstation.

The formulation that was presented in this subsection is a simple extension of the formalism that was developed in Ref. 29 for discussing the bulk effective conductivity or dielectric constant of a two-component periodic composite when both components are electrically isotropic and there is no magnetic field present.

Since the subsequent discussions are all confined to the case where the host (i.e., the No. 2 component) is an isotropic, free-electron-like metal and the inclusions (i.e., the No. 1 component) are perfect insulators, the most important parameter is the Hall to Ohmic resistivity ratio $\rho_H/\rho$. We will henceforth denote this dimensionless parameter by $H$. In a free-electron metal we can thus write

$$H \equiv \frac{\rho_H}{\rho} = \omega_c \tau, \tag{2.37}$$

where $\omega_c = e\mathcal{H}/mc$ is the cyclotron frequency, $\tau$ is the conductivity relaxation time, and $\mathcal{H}$ is the magnitude of the magnetic field in conventional units.

### C. The convergence problem

Use of the series (2.33) for calculating $F_{\alpha\beta}(1)$ is hindered by the fact that $s = 1$ is often outside the radius of convergence. Roughly speaking, this is due to the fact that the denominator in the expression (2.25) for $\Gamma_{\mathbf{gg}'}$ only depends on the symmetric part of $\hat{\sigma}_2$, and, therefore, decreases as $H^{-2}$ for strong fields, whereas the numerator depends on all parts of $\delta\hat{\sigma}$, including the antisymmetric part (when $\mathbf{g} \neq \mathbf{g}'$) which only decreases as $H^{-1}$. Therefore, the matrix elements $\Gamma_{\mathbf{gg}'}$, $\mathbf{g} \neq \mathbf{g}'$ increase as $H$ for large $H$, and consequently the radius of convergence of (2.33) is expected to decrease as $H^{-1}$.

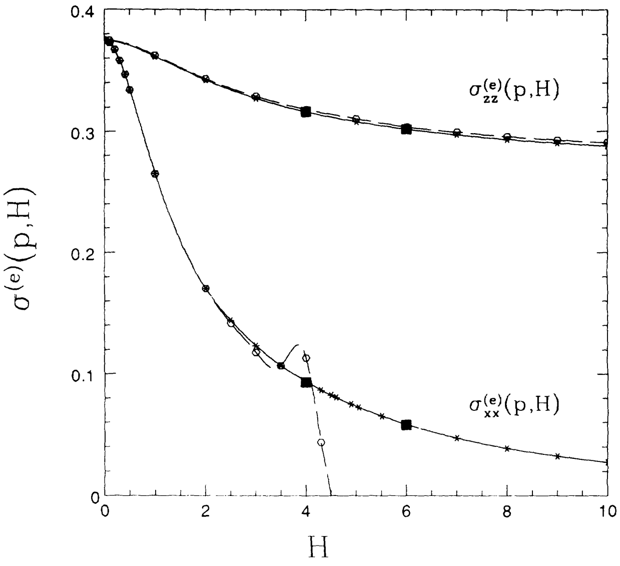

FIG. 3. Components $\sigma^{(e)}_{xx}$ and $\sigma^{(e)}_{zz}$ of the effective magnetoconductivity tensor for the same sample as in Fig. 5, plotted as functions of the dimensionless magnetic field $H$. Three different techniques are compared for obtaining results from the series expansion (2.33) for $F_{\alpha\beta}(s)$: Results obtained by a straightforward summation of the power series in $1/s$ for $F_{\alpha\beta}(s = 1)$ are shown as empty hexagons connected by dashed lines. Results obtained by summing the transformed power series in $1/w$ for $F_{\alpha\beta}[s(w = 1)]$ are shown as solid squares. Results obtained by applying the Padé method to the original series (2.33) are shown as asterisks connected by solid lines.

We employed two different stratagems in order to try and sum the series when it was in fact divergent: (a) reexpansion of the function $F_{\alpha\beta}(s)$ around a finite value $s_0$ instead of around $s = \infty$, (b) Padé analysis based on the divergent series (2.33). Results obtained using both of these approaches are shown in Fig. 3, along with results from a straightforward summation of the original series.

Reexpansion was based upon a fractional linear transformation to a new variable $w(s)$ (see Fig. 4)

$$\frac{1}{w} = \frac{s_0 - s}{s + s_0 - 2}, \quad s_0 > 1, \tag{2.38}$$

and substitution of the expansion of $1/s$ in powers of $1/w$ (note that $w = 1$ corresponds to $s = 1$)

$$\frac{s_0}{s} = 1 + \frac{2(1 - \frac{1}{s_0})}{w} \sum_{n=0}^{\infty} \left( \frac{1 - \frac{2}{s_0}}{w} \right)^n \tag{2.39}$$

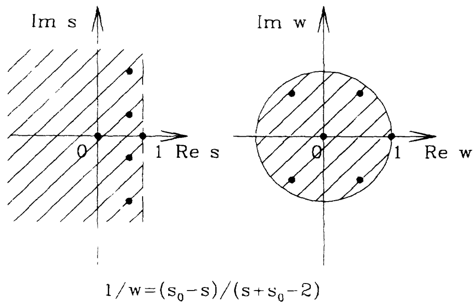

FIG. 4. Schematic drawing of the fractional linear transformation from $s$ to $w$ [see (2.38)]. The singularities that were located inside a rectangular strip in the $s$ plane are transformed so as to lie inside the unit circle in the $w$ plane.

in (2.33). The new series for $F_{\alpha\beta}[s(w)]$ in powers of $1/w$ was then tested for convergence at $w = 1$ and summed there. In practice, the result of this procedure depends upon $s_0$, even though $F_{\alpha\beta}(1)$ should not. The value used for $s_0$ was, therefore, chosen to lie in a range where the dependence upon it is flat (see Figs. 5 and 6). The existence of such a plateau was one of the main criteria for the validity of this procedure. From Fig. 3 it is evident that reexpansion allowed results to be obtained for values of $H$ for which the original series diverges. Nevertheless, for $H > 6$ even this procedure failed to give reliable results when only 20 terms were available in (2.33).

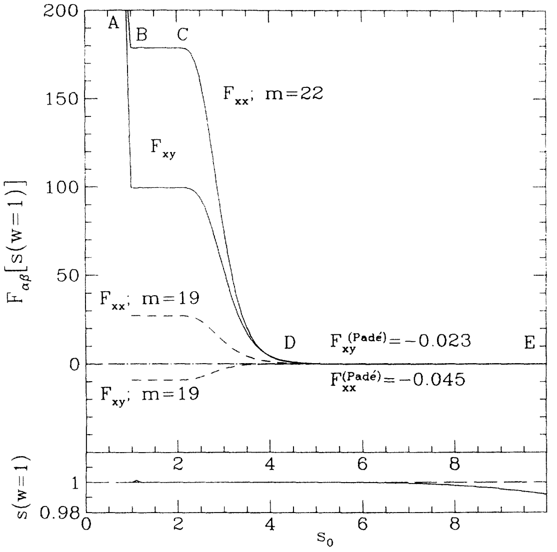

FIG. 5. Upper part: Results for $F_{xx}[s(w = 1)]$ and $F_{xy}[s(w = 1)]$ of a simple cubic array of insulating spheres with volume fraction $p_1 = 0.5$, embedded in a uniform, free-electron host with resistivity tensor given by (3.1) and $H = 6$. A truncated $\hat{\Gamma}$ matrix was used that included rows and columns corresponding to all **g** vectors with integer components running from $-N$ to $+N$ in all directions, with $N = 10$. This resulted in a $\hat{\Gamma}$ matrix of size $n \times n$ with $n = (2N + 1)^3 - 1 = 9260$. The results were obtained by computing the series expansion of $F_{\alpha\beta}(s)$ [see (2.33)], then using the transformation (2.38) to reexpand $F_{\alpha\beta}(s)$ in powers of $1/w$ and summing $m$ terms in the resultant series. The results are plotted vs the reexpansion parameter $s_0$ for $m = 19$ and $m = 22$. For $s_0 < 1$ the transformed series diverges at $w = 1$ (see the branch AB in the figure). For $1 < s_0 < 4$, the sum does not converge with increasing $m$ up to $m = 22$ [compare the dashed ($m = 19$) and solid ($m = 22$) lines], but in the lower part of that range, when $1 < s_0 < 2$, the sum of a given number of terms $m$ is independent of $s_0$ (see $BC$). For $4 < s_0 < 5$, the sum converges with increasing $m$ but to a value which depends strongly on $s_0$ (see the high $s_0$ part of the branch $CD$), and hence can have no physical meaning. Only when $s_0 > 5$ do we find both good convergence with increasing $m$ and a flat plateau as function of $s_0$. In that region we also find excellent agreement with the results of the Padé method. At even larger values of $s_0$, not shown in this figure, the results from summing the new series for $F_{\alpha\beta}[s(w = 1)]$ become unreliable when the above quoted values are used for $m$. Using higher values for $m$, i.e., summing more terms of the series, we can get good results even then. Lower part: The value of $s(w = 1)$ as calculated by summing $m = 22$ terms in the series (2.39), plotted vs $s_0$. For $s_0 > 7$, this value begins to deviate from 1, though the deviation is less than 1% up to $s_0 = 10$.

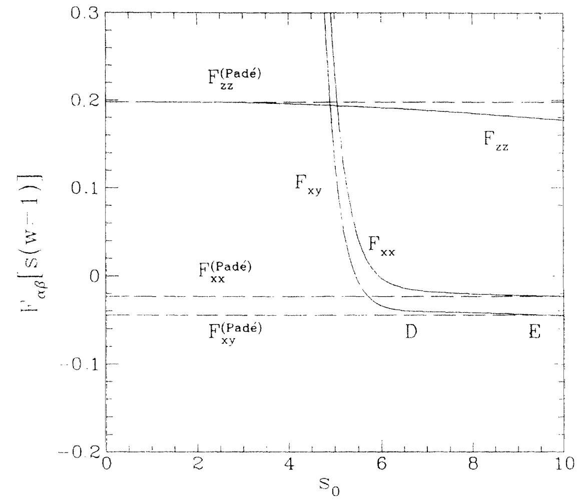

FIG. 6. The solid lines show results for $F_{xx}[s(w = 1)]$, $F_{xy}[s(w = 1)]$, and $F_{zz}[s(w = 1)]$ as functions of the reexpansion parameter $s_0$, calculated for the same sample and using the same parameters and the same method as in Fig. 5, but using an expanded scale for the ordinate axis. The flat plateau (see $DE$) begins when $s_0 \approx H$ and agrees with the values obtained using the Padé method, which are also shown in this figure as horizontal dashed lines.

Padé analysis (see Refs. 30 and 31) of the series (2.33) turned out to give reliable results even beyond that point (see Fig. 3), and was, therefore, used the most extensively. From calculations of the complete Padé table for some cases we reached the empirical conclusion that the diagonal approximants $[L/L] = P_L(z)/Q_L(z)$ converged best, where $z \equiv 1/s$ and $P_L(z)$, $Q_L(z)$ are degree $L$ polynomials which are constructed so as to satisfy

$$Q_L\left(\frac{1}{s}\right) F_{\alpha\beta}(s) - P_L\left(\frac{1}{s}\right) = O\left(\frac{1}{s^{2L+1}}\right) \qquad (2.40)$$

$$Q_L(0) = 1. \qquad (2.41)$$

An example of the complete Padé table for values of $\sigma_{xx}^{(e)}$ is presented in Table I for $H = 5$ and $p_1 = 0.5$.

Results from using these approximants are also shown in Figs. 3, 5, and 6. These figures show good agreement between the two methods for summing the divergent series whenever the reexpansion approach worked well. Figure 3 also shows that the Padé approach continues to work well even for higher magnetic fields, where the reexpansion method fails with the same number of terms available in (2.33). With 20 such terms available, we found that we could use the Padé method effectively up to quite large values of $H$. Such results are shown in Fig. 7, where components of the bulk effective resistivity

TABLE I. Complete $[L/M]$ Padé Table for $\sigma_{xx}^{(e)}$, obtained from a 20 term series expansion, of a simple cubic array of insulating spheres ($\hat{\sigma}_1 = 0$) with volume fraction $p_1 = 0.5$ embedded in a free-electron host with $\rho = 1$, $\rho_H = 5$. The magnetic field was along the $z$ axis. The boxes serve to highlight the diagonal approximants $[L/L]$, which exhibit the best convergence.

| $L\backslash M$ | 1 | 2 | 3 | 4 | 5 | 6 | 7 | 8 | 9 | 10 |
|---|---|---|---|---|---|---|---|---|---|---|
| 1 | $\boxed{0.12833}$ | 0.07295 | 0.07038 | 0.08358 | 0.09614 | 0.07093 | 0.05232 | 0.05361 | 0.12279 | 0.07033 |
| 2 | 0.09350 | $\boxed{0.07012}$ | 0.07244 | 0.13506 | 0.08673 | 0.25992 | 0.05348 | 0.05224 | -0.00818 | 0.23894 |
| 3 | 0.15801 | 0.07850 | $\boxed{0.08643}$ | 0.07704 | 0.07421 | 0.07219 | 0.07071 | 0.06955 | 0.06897 | 0.06929 |
| 4 | 0.06525 | 0.08238 | 0.08023 | $\boxed{0.07325}$ | 0.06972 | 0.06682 | 0.06287 | 0.06828 | 0.06917 | 0.06877 |
| 5 | 0.05315 | 0.07860 | 0.08648 | 0.07077 | $\boxed{0.06620}$ | 0.05626 | 0.06609 | 0.07500 | 0.06998 | 0.06964 |
| 6 | 0.09670 | 0.07296 | 0.05394 | 0.06898 | 0.06018 | $\boxed{0.06555}$ | 0.06920 | 0.06885 | 0.06932 | 0.06956 |
| 7 | 0.10598 | 0.06762 | 0.06526 | 0.06763 | 0.06766 | 0.07067 | $\boxed{0.06884}$ | 0.06906 | 0.07139 | 0.07070 |
| 8 | -0.07370 | 0.06591 | 0.06633 | 0.06766 | 0.06763 | 0.06921 | 0.06925 | $\boxed{0.07083}$ | 0.07068 | 0.06939 |
| 9 | 0.00185 | 0.06647 | 0.06491 | 0.06452 | 0.06561 | 0.06926 | 0.06920 | 0.07068 | $\boxed{0.07091}$ | 0.07033 |
| 10 | 0.00000 | 0.06735 | 0.06453 | 0.06484 | 0.06473 | 0.06966 | 0.06603 | 0.07033 | 0.07034 | $\boxed{0.07059}$ |

tensor $\hat{\rho}_e = \hat{\sigma}_e^{-1}$ for the same sample are plotted for $H$ in the range 0–32.

The convergence properties of (2.33) are of course governed by the mathematical singularities of $F_{\alpha\beta}(s)$. A discussion of those singularities and their effect on the convergence properties is given in Appendix A.

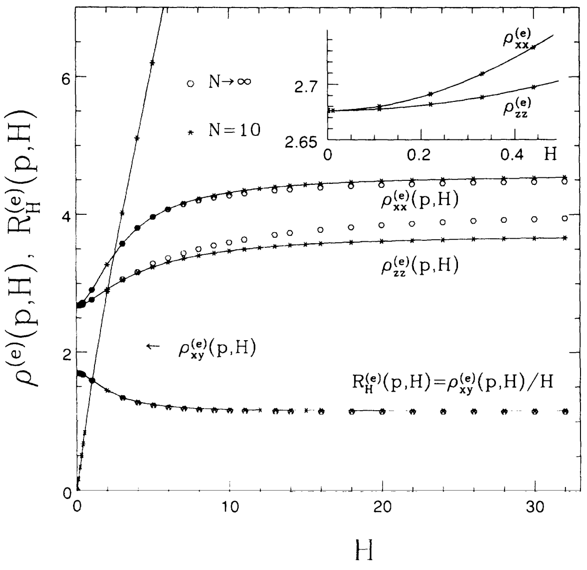

FIG. 7. Components $\rho_{xx}^{(e)}(p_1, H)$, $\rho_{xy}^{(e)}(p_1, H)$, $\rho_{zz}^{(e)}(p_1, H)$ of the bulk effective resistivity tensor $\hat{\rho}_e = 1/\hat{\sigma}_e$ and the Hall coefficient $R_H^{(e)}(p_1, H) = \rho_{xy}^{(e)}(p_1, H)/H$, plotted vs the magnetic field $H$. The sample is the same as in Fig. 5, and likewise for all the parameters with the exception of $H$ and $N$ ($N$ defines the range of **g** vectors used—see caption of Fig. 5). The asterisks denote results obtained using the Padé method and $N = 10$, while the hexagons denote results obtained by extrapolating from $N = 9$, 10 to $N = \infty$. The inset shows a magnified view of the plot of $\rho_{xx}^{(e)}(H)$ and $\rho_{zz}^{(e)}(H)$ near $H = 0$, showing that both curves are parabolic.

## III. TECHNICAL DETAILS AND RESULTS FOR VARIOUS MICROSTRUCTURES

We made detailed calculations of the bulk effective magnetoconductivity tensor $\hat{\sigma}_e$, and subsequently of its inverse $\hat{\rho}_e = 1/\hat{\sigma}_e$, for a variety of composites with a simple cubic periodic microstructure. Even if all the components were free-electron-like in that they exhibited a Hall resistivity but had an Ohmic resistivity which was a scalar and independent of $H$, we invariably found that the composite did have field dependent Ohmic components of the resistivity tensor. At strong fields, i.e., when $H \equiv \rho_H/\rho > 1$, this magnetoresistance exhibited a spectacular dependence on the direction of the magnetic field vector **H**—this was already reported and discussed in detail in Ref. 2. Here we will confine our discussion to the case where **H** points along the (001) direction, also called the $z$ axis, and to components of $\hat{\rho}_e$ and $\hat{\sigma}_e$ which also lie along the principal cubic axes. We will consider insulating inclusions of various shapes, always arranged in a simple cubic array and embedded in a free-electron-like conducting host medium with resistivity and conductivity tensors given by

$$\hat{\rho}_2 = \begin{pmatrix} 1 & -H & 0 \\ H & 1 & 0 \\ 0 & 0 & 1 \end{pmatrix}, \tag{3.1}$$

$$\hat{\sigma}_2 = \frac{1}{\hat{\rho}_2} = \begin{pmatrix} \frac{1}{1+H^2} & \frac{H}{1+H^2} & 0 \\ -\frac{H}{1+H^2} & \frac{1}{1+H^2} & 0 \\ 0 & 0 & 1 \end{pmatrix}. \tag{3.2}$$

This is tantamount to assuming that the Ohmic resistivity of the host medium is one, its Hall resistivity is $H$, and the magnetic field is directed along the positive $z$ axis. The different unit cell microgeometries that we considered are shown in Figs. 1 and 8, and they include a case where neighboring spherical inclusions overlap.

In order to proceed with the calculation we need the values of $\theta_{\mathbf{g}}$, which depend on the geometric form of the inclusions and on their relative positions. Explicit ex-

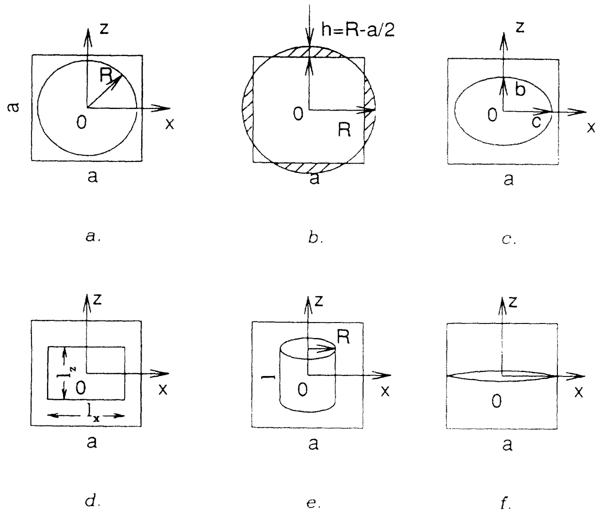

FIG. 8. The different cubic unit cells, of edge $a$, which were used in our calculations: (a) single sphere of radius $R$ which is less than $a/2$ (nonoverlapping), (b) single sphere of radius $R$ which is larger than $a/2$ but less than $a/\sqrt{2}$ (overlapping), (c) single ellipsoid with semi-axes $b$, $c$, $d$, all less than $a/2$ (nonoverlapping), (d) single rectangular prism of dimensions $l_x \times l_y \times l_z$, all less than $a/2$ (nonoverlapping), (e) single cylinder of radius $R < a/2$ (nonoverlapping) and length $l \leq a$, (f) single parabolic lens $\rho^2 + z = l^2$ (nonoverlapping). The formulas for $\theta_{\mathbf{g}}$ corresponding to all of these unit cells are given in Table II.

pressions for $\theta_{\mathbf{g}}$ are given in Table II and derived in Appendix B. We must distinguish between the case where the inclusions overlap and the case where they do not. In the case of a cubic array of spherical inclusions, neighboring spheres will just touch each other when the radius $R$ satisfies $R = a/2$, where $a$ is the lattice constant, which occurs at a volume fraction $p_1 = \pi/6 \approx 0.524$. At higher values of $p_1$ the spheres overlap and a different expression must be used for $\theta_{\mathbf{g}}$ (see Table II). The host medium continues to percolate up to the value $p_1 = 0.965$, and that is, therefore, the conductivity threshold for such a system if the spheres are insulating. However, if the inclusions were conducting while the host material was a perfect insulator, then the conductivity threshold would be at $p_1 = 0.524$. Our theory is applicable to both cases, but the latter case will be discussed elsewhere.[32] We note only that the scheme presented here is not invariant under the interchange $\hat{\sigma}_1 \leftrightarrow \hat{\sigma}_2$: We cannot allow $\hat{\sigma}_2 = 0$ in our theory because $\hat{\sigma}_2$ appears in the denominator of certain expressions [see (2.33), (2.34)]. Moreover, for very small values of $\hat{\sigma}_2$ the series (2.33) diverges even for $H = 0$, and the correct value of $\hat{\sigma}^{(e)}$ is obtained only by using a Padé procedure. It is better, therefore, to assign the roles of host and inclusions in such a way that the resistivity of the host medium is less than that of the inclusions. Thus, if the conductivity of the spherical inclusions is higher than the conductivity of the matrix material, we should switch the roles of the inclusions and the host material. When we do this, $\theta_{\mathbf{g}}$ must be replaced by the Fourier transform of the characteristic function of the other component, which is equal to $\delta_{\mathbf{g}0} - \theta_{\mathbf{g}}$.

### A. Simple cubic array of nonoverlapping spheres

This model is perhaps the simplest kind of periodic composite. The Fourier coefficients of $\theta_1(\mathbf{r})$ are easily calculable in closed form

$$\theta_{\mathbf{g}} = \frac{4\pi}{(|\mathbf{g}|a)^3}[\sin(|\mathbf{g}|R) - |\mathbf{g}|R\cos(|\mathbf{g}|R)] \equiv \theta_{\mathbf{g}}^{(\text{sphere})}, \tag{3.3}$$

TABLE II. Expressions for $\theta_{\mathbf{g}}$ for different types of unit cell in a simple cubic lattice.

| Figure | $\theta_{\mathbf{g}} = \frac{1}{V_a}\int_{V_a} \theta_1(\mathbf{r}) e^{-i\mathbf{g}\cdot\mathbf{r}} dV$ |
|---|---|
| Nonoverlapping sphere, see Fig. 8(a) | $\theta_{\mathbf{g}} = \left[4\pi/(\vert g\vert a)^3\right] [\sin(\vert g\vert R) - \vert g\vert R\cos(\vert g\vert R)]$<br>$\equiv \theta_{\mathbf{g}}^{(\text{sphere})}$ |
| Overlapping sphere see Fig. 8(b) | $\theta_{\mathbf{g}} = \theta_{\mathbf{g}}^{(\text{sphere})} - \theta(R - a/2)[\mathcal{I}(g_\perp^{(xy)}, g_z, R, a) + \mathcal{I}(g_\perp^{(zx)}, g_y, R, a) + \mathcal{I}(g_\perp^{(yz)}, g_x, R, a)]$,<br>where<br>$\mathcal{I}(g_\perp, g_z, R, a) = [4\pi/(a^3 g_\perp)] \int_{a/2}^{R} dz \sqrt{R^2 - z^2} J_1(g_\perp \sqrt{R^2 - z^2})\ \cos(\vert g_z\vert z)$;<br>$\mathcal{I}(0, g_z, R, a) = (4\pi/a^3\vert g_z\vert^3)\{[\sin(\vert g_z\vert R) - \vert g_z\vert R\ \cos(\vert g_z\vert R)]$<br>$- \left[\sin(\vert g_z\vert \frac{a}{2}) - \vert g_z\vert \frac{a}{2}\cos(\vert g_z\vert \frac{a}{2})\right] - \frac{g_z^2}{2}(R^2 - \left(\frac{a}{2}\right)^2) \sin(\vert g_z\vert \frac{a}{2})\}$;<br>$\mathcal{I}(0, 0, R, a) = 2\pi h^2(3R - h)/(3a^3)$, $g_\perp^{(xy)} = \sqrt{g_x^2 + g_y^2}$; $h = R - a/2$. |
| Ellipsoid<br>$(x/b)^2 + (y/c)^2 + (z/d)^2 = 1$<br>see Fig. 8(c) | $\theta_{\mathbf{g}} = 4\pi bcd[\sin(\tilde{g}) - \tilde{g}\cos(\tilde{g})]/(\tilde{g}a)^3$,<br>where<br>$\tilde{g} = \sqrt{b^2 g_x^2 + c^2 g_y^2 + d^2 g_z^2}$ |
| Rectangular prism see Fig. 8(d) | $\theta_{\mathbf{g}} = (2/a)^3 [\sin(g_x l_x/2)/g_x] [\sin(g_y l_y/2)/g_y] [\sin(g_z l_z/2)/g_z]$ |
| Cylinder see Fig. 8(e) | $\theta_{\mathbf{g}} = [4\pi/(a^3 g_\perp)] R J_1(R g_\perp) [\sin(\vert g_z\vert l/2)/\vert g_z\vert]$,<br>where $J_1(x)$ is a Bessel function and $g_\perp = \sqrt{g_x^2 + g_y^2}$ |
| Parabolic lens with profile $\rho^2 + az = l^2$ see Fig. 8(f) | $\theta_{\mathbf{g}} = [2\pi/(a^2 g_z^2)] U_2(2l^2 g_z/a, l g_\perp)$,<br>where $U_2(x, y)$ is a Lommel function of two variables<br>(see Ref. 34) |

where $R$ is the radius of the spheres, $a$ is the linear size of the unit cell, and $\mathbf{g} = \frac{2\pi}{a}(n_x, n_y, n_z)$ with $n_x, n_y, n_z$ as arbitrary integers is a reciprocal lattice vector. In order to truncate the infinite set of $\mathbf{g}$ vectors, we allowed the integers $n_x$, $n_y$, and $n_z$ to range from $-N$ to $+N$. The $A^{(r)}_{\alpha\beta}$ matrices of (2.34) were calculated for $r \leq 20$ using values of $N$ as high as 10, and were then extrapolated to $N = \infty$ from the two highest values of $N$ by assuming that the $N$ dependence has the form

$$A^{(r)}_{\alpha\beta}(N) = A^{(r)}_{\alpha\beta}(\infty) + B/N. \tag{3.4}$$

The extrapolated values were used to calculate $F_{\alpha\beta}(1)$ from the series expansion (2.33) with the help of Padé tables. The values obtained using the extrapolation of (3.4) are shown in Fig. 7 by hexagons, and the values obtained for $N = 10$ are shown by asterisks connected by a solid line. Evidently, using 21 reciprocal lattice vectors in each direction (i.e., $N = 10$) is good enough for calculating $\rho_{xx}(p_1, H)$, $\rho_{xy}(p_1, H)$, and the Hall coefficient $R_H(p_1, H)$ accurately. The same cannot be said of $\rho_{zz}(p_1, H)$, where there are significant differences between the $N = 10$ results and the $N = \infty$ extrapolations. To get more accurate results one should increase the value of $N$, with a corresponding price in increased computation time.

The effective resistivity components $\rho^{(e)}_{xx}(p_1, H)$, $\rho^{(e)}_{xy}(p_1, H)$, $\rho^{(e)}_{zz}(p_1, H)$, and the effective Hall coefficient $R^{(e)}_H(p_1, H) = \rho^{(e)}_{xy}(p_1, H)/H$ are shown in Fig. 7 as functions of the dimensionless magnetic field $H$. Clearly, there is a strong dependence on $H$ at low and intermediate values of $H$ but saturation occurs when $H > 10$. The scaling behavior becomes evident if we plot these functions of $H$ in log-log graphs (see Figs. 9 and 10). For low fields, the diagonal components of $\hat{\rho}_e(p_1, H) - \hat{\rho}_e(p_1, 0)$ are all proportional to $H^2$ (see Fig. 9) and the same is true for the difference in effective Hall coefficients $R^{(e)}_H(p_1, 0) - R^{(e)}_H(p_1, H)$ (see Fig. 10). This low-field behavior is similar to what was found in calculations on disordered composites.[13] The character of the saturation at high fields is also similar to what was found in calculations on disordered composites.[27,28]

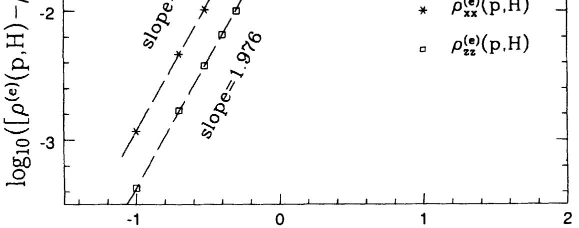

FIG. 9. Log-log plot of the ohmic components $\rho^{(e)}_{xx}(p_1, H)$ and $\rho^{(e)}_{zz}(p_1, H)$ of the bulk effective resistivity tensor vs $H$. The sample, as well as all parameters except $H$, are the same as in Fig. 5. The values of the dimensionless magnetic field range from $H = 0.1$ up to $H = 32$.

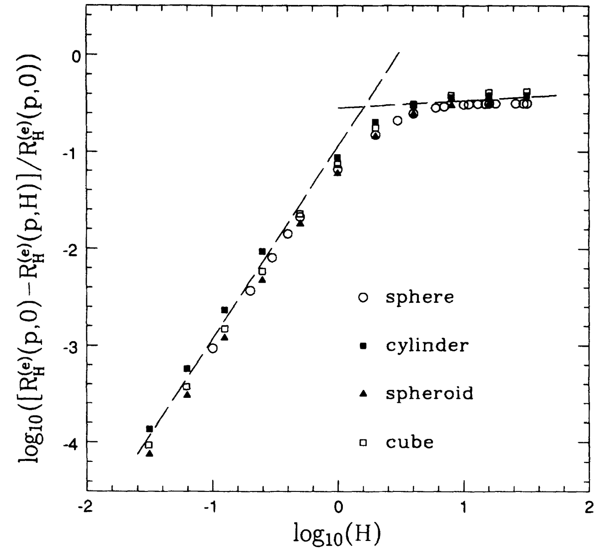

FIG. 10. Log-log plot of the effective Hall coefficient $R^{(e)}_H(p_1, H) = \rho^{(e)}_{xy}(p_1, H)/H$ calculated for a simple cubic array of insulating inclusions with different shapes, but all with the same volume fraction $p_1 = 0.5$ and unit cell edge $a = 1$. The linear sizes of the different inclusions are: sphere radius $R = 0.492$; cylinder radius $R = 0.43$, cylinder height $l_z = 2R = 0.86$; spheroidal semiaxes $b = 0.477$, $c = d = 0.5$ (oblate spheroid); cube edges $l_x = l_y = l_z = 0.5^{1/3} = 0.794$. The values of the dimensionless magnetic field range from $H = 2^{-5} = 0.03125$ up to $H = 2^5 = 32$. All the other parameters are the same as in Fig. 5.

### B. Other types of nonoverlapping inclusions and other microstructures

Since it might be difficult to fabricate periodic composite materials where the inclusions have a precisely spherical shape, we considered other shapes too: nonoverlapping spheroids, cylinders, rectangular prisms, etc. (see Fig. 8). All of these shapes have in common that, when there is no overlap between different inclusions, the $\theta_{\mathbf{g}}$ function can be calculated in analytical closed form in terms of elementary functions. The expressions for that function in the above mentioned cases appear in Table II, where we also present our result for the case of a simple cubic array of spheres where nearest neighbors do overlap. Results for the relative change of the Hall coefficient with $H$ are shown as a log-log plot in Fig. 10 for four different shapes of nonoverlapping inclusions, all arranged as a simple cubic array with the same volume fraction $p_1 = 0.5$. We do not include the case of a parabolic lens shape in this figure, because inclusions of that shape overlap when $p_1 = 0.5$. From Fig. 10 it is clear that the low-field behavior, as well as the saturation at high magnetic fields, do not depend strongly on the detailed shapes of the inclusions. This behavior suggests that perhaps $R_H^{(e)}$ of a disordered composite with a similar composition will also behave in much the same way as function of $H$.

### C. Overlapping spheres

For this case, calculation of the Fourier coefficients of $\theta_1(\mathbf{r})$ is more complicated than in the nonoverlapping case [see (3.3)]. In Ref. 29 the coefficients $\theta_{\mathbf{g}}$ for a simple cubic array of overlapping spheres were calculated using three-dimensional (3D) numerical integration. However, it is possible to perform a considerable portion of the calculation analytically as long as $R \le a/\sqrt{2}$, when only nearest neighbor spheres overlap. To show this, we first note that the volume integral can be divided into several parts

$$\theta_{\mathbf{g}} = \frac{1}{a^3}\int_{V_a} dV e^{-i\mathbf{g}\cdot\mathbf{r}} = \theta_{\mathbf{g}}^{(\text{sphere})} - \sum_{i=1}^{6}\theta_{i,\mathbf{g}}, \qquad (3.5)$$

where $\theta_{\mathbf{g}}^{(\text{sphere})}$ is the Fourier integral over the *entire* sphere of radius $R > a/2$ [i.e., the expression which is given by (3.3)], while $\theta_{i,\mathbf{g}}$ are the integrals over the six sections of that sphere which protrude outside the cubic unit cell [see Fig. 8(b)]. These six terms are similar, and involve an integral with a high degree of symmetry. Once we have calculated one of the terms, say $\theta_{1,\mathbf{g}}$, for all possible wave vectors $\mathbf{g} = (g_x, g_y, g_z)$, then all the other terms $i = 2...6$ can be found by applying appropriate rotation transformations to the vector $\mathbf{g}$. It is convenient to denote the sum of integrals from two diametrically opposed protrusions by $\mathcal{I}(g_\perp^{(xy)}, g_z, R, a)$, etc., where $g_\perp^{xy} \equiv \sqrt{g_x^2 + g_y^2}$. We can then write

$$\begin{aligned}\theta_{\mathbf{g}} &= \theta_{\mathbf{g}}^{(\text{sphere})} - [\mathcal{I}(g_\perp^{(xy)}, g_z, R, a) \\ &\quad + \mathcal{I}(g_\perp^{(zx)}, g_y, R, a) + \mathcal{I}(g_\perp^{(yz)}, g_x, R, a)] \\ &= I(g_\perp^{(xy)}, g_z, R, a) + I(g_\perp^{(zx)}, g_y, R, a) \\ &\quad + I(g_\perp^{(yz)}, g_x, R, a) - 2\theta_{\mathbf{g}}^{(\text{sphere})}, \qquad (3.6)\end{aligned}$$

where

$$\begin{aligned}I(g_\perp, g_z, R, a) \equiv \frac{4\pi}{a^3 g_\perp}\int_0^{a/2} dz \sqrt{R^2 - z^2} J_1 \\ \times (g_\perp \sqrt{R^2 - z^2}) \cos(g_z z). \qquad (3.7)\end{aligned}$$

The expression for $\mathcal{I}(g_\perp, g_z, R, a)$ is the same as (3.7), except that the limits of integration are from $a/2$ to $R$. $J_1(x)$ is the usual Bessel function of order one. For the particular case $g_\perp = 0$, the integral (3.7) can easily be evaluated in terms of elementary functions (see Appendix B and Table II). For arbitrary nonzero values of $g_\perp$, the situation is more complicated. However, we can calculate the integral $I(g_\perp, g_z, R, a)$ numerically using either some standard, 1D numerical integration algorithm, which is much more efficient and accurate than 3D numerical integration, or else an appropriate (double) series expansion

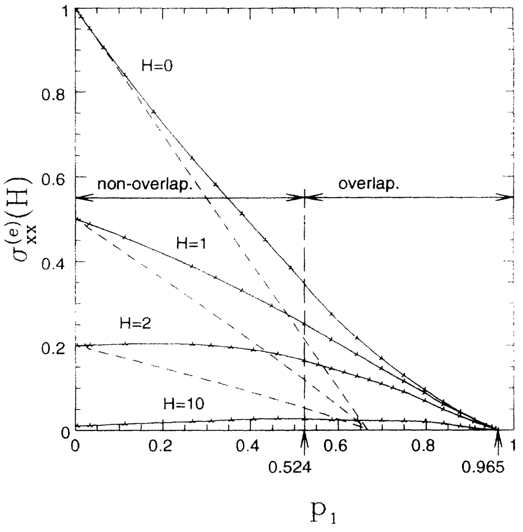

FIG. 11. The bulk effective magnetoconductivity tensor component $\sigma_{xx}^{(e)}(p_1, H)$ of a simple cubic array of insulating spheres embedded in a free-electron host with unit Ohmic resistivity plotted as function of the volume fraction of the spheres $p_1$ for various values of the dimensionless magnetic field $H$. Neighboring spheres overlap whenever $p_1 > 0.524$ and the system is an insulator for $p_1 > 0.965 = 1 - p_c$, where $p_c = 0.035$ is the percolation or connectivity threshold of the host component. All the other parameters are the same as in Fig. 5. The dashed lines represent results obtained from the effective medium approximation of Refs. 22 and 23.

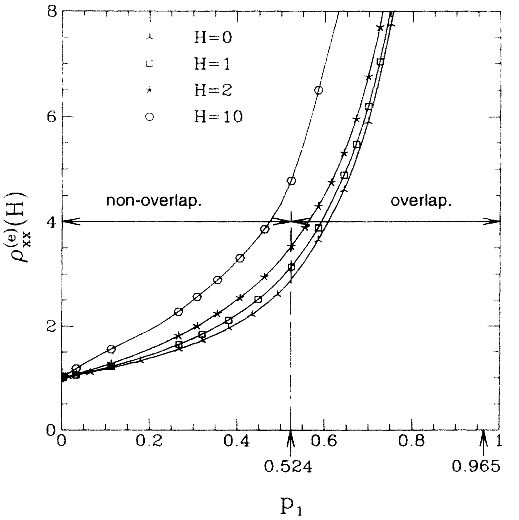

FIG. 12. Plot of the bulk effective magnetoresistivity tensor component $\rho_{xx}^{(e)}(p_1, H)$ vs $p_1$ for the same set of samples and parameters as in Fig. 11.

(see Appendix B).

Using this approach, we calculated the $xx$ components of the conductivity (Fig. 11) and resistivity (Fig. 12) as functions of the insulator volume fraction for cubic arrays of insulating spheres over the entire range of volume fractions up to $p_1 = 0.965$ and for various values of the magnetic field $H$. The spheres begin to overlap as soon as the volume fraction increases above $p_1 = 0.523$ (corresponding to $R = a/2$). When $p_1$ rises above the conductivity threshold $p_1 = 0.965$ (corresponding to $R = a/\sqrt{2}$), the conductivity vanishes.

## IV. DISCUSSION AND SUMMARY

We presented a method for calculating the bulk effective Ohmic and Hall resistivities of periodic composites at arbitrary values and directions of the magnetic field $\mathbf{H}$. In this article we applied the method to a restricted set of systems: simple cubic arrays of perfectly insulating inclusions embedded in a free-electron-like conducting host with $\mathbf{H}$ along a principal cubic axis. The method is however applicable to any kind of periodic, multicomponent composite medium, with the magnetic field pointing in any direction, and all components of the resistivity tensor are calculable.

We presented detailed results of calculations for the transverse Ohmic resistivity component $\rho_{xx}^{(e)}$ and transverse Ohmic conductivity component $\sigma_{xx}^{(e)}$ as functions of the volume fraction $p_1$ of the inclusions for the case of a simple cubic array of insulating spheres, when the magnetic field is along the $z$ axis. We also presented detailed results for the differences $\rho_{xx}^{(e)}(H) - \rho_{xx}^{(e)}(0)$, $\rho_{zz}^{(e)}(H) - \rho_{zz}^{(e)}(0)$ as functions of the dimensionless magnetic field strength $H$ for the same model, and for the difference $R_H^{(e)}(0) - R_H^{(e)}(H) \equiv [\rho_{xy}^{(e)}(0) - \rho_{xy}^{(e)}(H)]/H$ as function of $H$ for various shapes of inclusions. For nonoverlapping inclusions we found that for the same value of $p_1$, the dependance of $R_H^{(e)}$ on $H$ is insensitive to the precise shape of the inclusions. At low and intermediate values of $H$, all three of the above mentioned differences depend strongly upon $H$, increasing as $H^2$. When $H$ is large enough so that the Hall resistivity of the host becomes comparable to its Ohmic resistivity, this rate of increase begins to level off and eventually, when $H \equiv \rho_H/\rho > 10$, saturation sets in.

Some other interesting phenomena in this system are (a) strong oscillations of $\rho_{xx}^{(e)}(\mathbf{H})$ and $\rho_{zz}^{(e)}(\mathbf{H})$ with changing direction of $\mathbf{H}$—this was reported earlier,[2] (b) critical behavior of the magnetotransport near a conductivity threshold in a periodic composite—this will be discussed elsewhere.[32]

In the Appendices we showed how to construct bounds for the locations of the singularities of $F_{\alpha\beta}(s)$—important information to have when trying to calculate physical quantities like $\hat{\sigma}_e$ from a divergent power series. We also presented details of an efficient and accurate series expansion method for calculating the Fourier coefficients $\theta_{\mathbf{g}}$ for a system of overlapping spheres. This should be useful also for calculating other physical properties of such composite systems.

## ACKNOWLEDGMENTS

This research was supported in part by grants from the U.S.-Israel Binational Science Foundation, the Israel Science Foundation, and the Center for Absorption in Science of the Science Ministry of the State of Israel. This work was completed while D.J.B. was visiting the University of Cologne.

## APPENDIX A: ANALYTICAL PROPERTIES OF $F_{\alpha\beta}(s)$

In order to analyze the analytic properties of $F_{\alpha\beta}(s)$, we need to have some estimates for its singularities. From (2.33) we see that those singularities are just the eigenvalues of $\hat{\Gamma}$. Denoting the eigenvalues and eigenvectors of the $\Gamma_{\mathbf{g}\mathbf{g}'}$ matrix by $s_n$, $a_{\mathbf{g}}^{(n)}$, we have

$$s_n a_{\mathbf{g}}^{(n)} = \sum_{\mathbf{g}'\neq 0} \Gamma_{\mathbf{g}\mathbf{g}'} a_{\mathbf{g}'}^{(n)}. \tag{A1}$$

The matrix $\Gamma_{\mathbf{g}\mathbf{g}'}$ would be self-adjoint if the tensor $\delta\hat{\sigma}$ were symmetric. But in the presence of a magnetic field $\delta\hat{\sigma}$ is nonsymmetric, and consequently the eigenvalues $s_n$ are in general complex. However, because the integro-differential operator $\hat{\Gamma}$ is real, the eigenvalues always appear in complex conjugate pairs. This follows from the observation that if $\phi_n(\mathbf{r})$ is an eigenfunction of $\hat{\Gamma}$ with the eigenvalue $s_n$, then $\phi_n^*(\mathbf{r})$ is also an eigenfunction of $\hat{\Gamma}$ with the eigenvalue $s_n^*$.

Using (A1) and (2.25) we can get the following expression for $s_n$:

$$\begin{aligned} s_n \sum_{\mathbf{g}\neq 0} |a_{\mathbf{g}}^{(n)}|^2 &= \sum_{\mathbf{g}\neq 0} \sum_{\mathbf{g}'\neq 0} a_{\mathbf{g}}^{(n)*} \Gamma_{\mathbf{g}\mathbf{g}'} a_{\mathbf{g}'}^{(n)} \\ &= \sum_{\text{all } \mathbf{g}} \sum_{\text{all } \mathbf{g}'} \theta_{\mathbf{g}-\mathbf{g}'} \mathbf{b}_{\mathbf{g}}{}^{*} \cdot \delta\hat{\sigma} \cdot \mathbf{b}_{\mathbf{g}'}, \end{aligned} \tag{A2}$$

where

$$\mathbf{b}_{\mathbf{g}} \equiv \begin{cases} 0 & \text{for } \mathbf{g} = 0 \\ \frac{a_{\mathbf{g}}^{(n)} \mathbf{g}}{(\mathbf{g}\cdot\hat{\sigma}_{2s}\cdot\mathbf{g})^{1/2}} & \text{otherwise.} \end{cases} \tag{A3}$$

Defining $\mathbf{b}(\mathbf{r})$ as the vector function whose Fourier coefficients are $\mathbf{b}_{\mathbf{g}}$

$$\mathbf{b}(\mathbf{r}) \equiv \sum_{\mathbf{g}} \mathbf{b}_{\mathbf{g}} e^{i\mathbf{g}\cdot\mathbf{r}}, \tag{A4}$$

and taking the eigenvectors $a_{\mathbf{g}}^{(n)}$ to be normalized to one

$$\sum_{\mathbf{g}\neq 0} |a_{\mathbf{g}}^{(n)}|^2 = 1, \tag{A5}$$

we get

$$s_n = \frac{1}{V_a}\int_{V_a} dV\theta_1(\mathbf{r})\mathbf{b}^*(\mathbf{r})\cdot\delta\hat{\sigma}\cdot\mathbf{b}(\mathbf{r}) = \langle\theta_1\mathbf{b}^*\cdot\delta\hat{\sigma}\cdot\mathbf{b}\rangle. \tag{A6}$$

By writing $\delta\hat{\sigma}$ as a sum of symmetric and antisymmetric matrices $\delta\hat{\sigma}_s$, $\delta\hat{\sigma}_a$,

$$\delta\hat{\sigma} = \delta\hat{\sigma}_s + \delta\hat{\sigma}_a, \tag{A7}$$

we get a natural separation of $s_n$ into its real and imaginary parts

$$\mathrm{Re}(s_n) = \langle\theta_1\mathbf{b}^*\cdot\delta\hat{\sigma}_s\cdot\mathbf{b}\rangle, \tag{A8}$$

$$\begin{aligned} i\,\mathrm{Im}(s_n) &= \langle\theta_1\mathbf{b}^*\cdot\delta\hat{\sigma}_a\cdot\mathbf{b}\rangle = \langle\theta_1\mathbf{b}^*\cdot(\delta\vec{\lambda}\times\mathbf{b})\rangle,\\ &= \delta\vec{\lambda}\cdot\langle\theta_1(\mathbf{b}\times\mathbf{b}^*)\rangle, \end{aligned} \tag{A9}$$

where we have represented the $3\times3$ antisymmetric matrix $\delta\hat{\sigma}_a$ by an axial vector $\delta\vec{\lambda}$. From these results we can easily derive bounds for $\mathrm{Re}(s_n)$ and $\mathrm{Im}(s_n)$.

For the case where component No. 1 is an insulator, namely $\hat{\sigma}_1 = 0$, we get

$$0 < \mathrm{Re}(s_n) = \langle\theta_1\mathbf{b}^*\cdot\hat{\sigma}_{2s}\cdot\mathbf{b}\rangle < \langle\mathbf{b}^*\cdot\hat{\sigma}_{2s}\cdot\mathbf{b}\rangle \tag{A10}$$

$$= \sum_{\mathbf{g}}(\mathbf{b}^*_{\mathbf{g}}\cdot\hat{\sigma}_{2s}\cdot\mathbf{b}_{\mathbf{g}}) = \sum_{\mathbf{g}\neq0}|a^{(n)}_{\mathbf{g}}|^2 = 1. \tag{A11}$$

These bounds are rigorous.

A similarly rigorous upper bound for $|\mathrm{Im}(s_n)|$ is obtained as follows:

$$\begin{aligned} |\mathrm{Im}(s_n)| &= |\vec{\lambda}_2\cdot\langle\theta_1(\mathbf{b}\times\mathbf{b}^*)\rangle| = \left|\vec{\lambda}_2\cdot\frac{1}{V_a}\int_{V_a} dV\theta_1(\mathbf{b}\times\mathbf{b}^*)\right| < |\vec{\lambda}_2|\frac{1}{V_a}\int_{V_a} dV|\mathbf{b}|^2\\ &= |\vec{\lambda}_2|\sum_{\mathbf{g}}|\mathbf{b}_{\mathbf{g}}|^2 = |\vec{\lambda}_2|\sum_{\mathbf{g}\neq0}\frac{|a^{(n)}_{\mathbf{g}}|^2|\mathbf{g}|^2}{\mathbf{g}\cdot\hat{\sigma}_{2s}\cdot\mathbf{g}} \le \frac{|\vec{\lambda}_2|}{\sigma_{2,\min}}\sum_{\mathbf{g}\neq0}|a^{(n)}_{\mathbf{g}}|^2 = \frac{|\vec{\lambda}_2|}{\sigma_{2,\min}} = |H|, \end{aligned} \tag{A12}$$

where $\sigma_{2,\min}$ denotes the smallest eigenvalue of $\hat{\sigma}_{2s}$ and $\vec{\lambda}_2$ is the axial vector which represents the antisymmetric part of $\hat{\sigma}_2$. These estimates are in good agreement with numerical calculations of the eigenvalues $s_n$ (see Fig. 13).

We are interested in the regime of strong magnetic fields, where $|H| \ge 1$. The radius of convergence $r_c$ of (2.33) will be $1/|s_{\max}|$, where $s_{\max}$ is the eigenvalue of $\hat{\Gamma}$ that is farthest away from the origin. From (A11) and (A12) we would, therefore, estimate $r_c \approx 1/|H|$, which would mean that the series expansion for $F_{\alpha\beta}(1)$ would converge up to a field where $|H| \approx 1$. In practice, that series usually continues to converge up to a somewhat stronger field. Thus, in the case of a simple cubic array of insulating spherical inclusions (i.e., $\hat{\sigma}_1 = 0$) with a total volume fraction of $p_1 = 0.5$ embedded in a uniform conducting host medium, we found that the series for $F_{\alpha\beta}(1)$ converges up to a field strength where $H \approx 2$. This is due to the conservative nature of the strict inequalities in (A10) and (A12): we can probably expect the upper bounds on both $\mathrm{Re}(s_n)$ and $|\mathrm{Im}(s_n)|$ to be smaller by about a factor $p_1$, which in this case would increase the radius of convergence by a factor of 2. When trying to calculate $F_{\alpha\beta}(1)$ for stronger fields, the series expansion diverges.

The transformation $s \to w$ [see (2.38)] moves the singularities of $F_{\alpha\beta}(s)$ to the interior of the unit circle in the complex $w$ plane (see Fig. 4). Consequently, the expansion of $F_{\alpha\beta}[s(w)]$ in powers of $1/w$ will converge at $w = s = 1$. However, each coefficient of this series depends upon *all* coefficients of the series (2.33), and is, therefore, itself calculated by a truncated infinite sum. The accuracy with which the new coefficients are determined when a fixed number of terms are available in (2.33) may thus depend on the value of $s_0$. An argu-

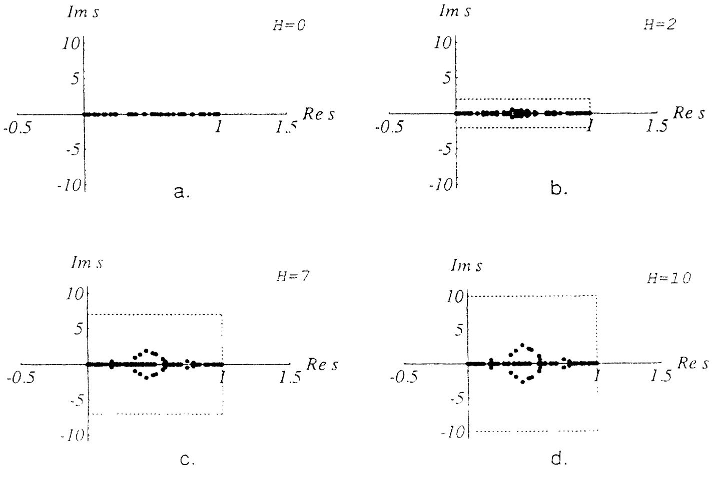

FIG. 13. Locations of the main eigenvalues $s_n$ (i.e., those that evoke the largest residues when $\hat{\sigma}_e$ is expanded as a sum of simple poles) of $\hat{\Gamma}$ in the complex $s$ plane calculated for a simple cubic array of insulating spherical inclusions ($\hat{\sigma}_1 = 0$) at $p_1 = 0.5$ for various magnetic field strengths (a) $H = 0$, (b) $H = 3$, (c) $H = 7$, (d) $H = 10$. The eigenvalues were obtained by numerically diagonalizing a finite, truncated version of the infinite $\hat{\Gamma}$ matrix, obtained by including $\mathbf{g}$ vectors with integer components ranging from $-N$ to $+N$ along each coordinate axis, with $N = 2$. This results in a truncated matrix of size $n\times n$, where $n = (2N+1)^3 - 1 = 124$. The theoretical bounds $0 < \mathrm{Re}(s) < 1, -H < \mathrm{Im}(s) < +H$ are shown in the figures as dotted rectangles.

ment for using a small value of $s_0$ is that if we used a value that was too large, then the transformation (2.38) would compress most of the complex $s$ plane, including the singular points of $F_{\alpha\beta}(s)$, into a very small neighborhood of $w = 1$ and that would adversely affect the rate of convergence at $w = 1$. On the other hand, $s_0$ must be large enough so that $1/s_0$ is within the radius of convergence of (2.33). In practice, we exploited the fact that $F_{\alpha\beta}[s(w = 1)] = F_{\alpha\beta}(s = 1)$ should be independent of $s_0$: plotting the result of summing a fixed number of terms $m$ in the series for $F_{\alpha\beta}[s(w = 1)]$ vs $s_0$ we looked for a broad plateau where the result is independent of $s_0$ (see Figs. 5 and 6, where results are shown for a simple cubic array of nonoverlapping spheres with $p_1 = 0.5$, embedded in a uniform, free-electron conducting host with $H = 6$ and the magnetic field pointing along a principal symmetry axis, called the $z$ axis). The best values of $s_0$ found in this way turned out to be fairly close to $H$. However, good results could only be obtained for $H$ up to about 6, when we used 20 terms in the power series (2.33) and $\mathbf{g}$ vectors ranging from $-10$ to $+10$ in all directions (see Fig. 3). We also found that by starting with a larger number of terms in (2.33) we could get reliable results with this approach even for higher values of $H$.

## APPENDIX B: EVALUATIONS OF $\theta_g$

Here we present the evaluation of the Fourier coefficients $\theta_{\mathbf{g}}$ for some geometrical shapes of inclusions, many of which have rotational symmetry around some axis (see Fig. 8). Let $OZ$ be such a symmetry axis, then we can write, using cylindrical coordinates in the integration,

$$\theta_{\mathbf{g}} = \frac{1}{a^3}\int_{-z_1}^{z_1} dz \int_0^{\rho(z)} d\rho\rho \times \int_0^{2\pi} d\phi e^{-ig_x\rho\cos\phi - ig_y\rho\sin\phi - ig_z z}, \tag{B1}$$

where $\rho(z)$ describes the surface of an inclusion with the above-mentioned symmetry. Using the transformation $g_x\cos\phi + g_y\sin\phi = g_\perp\cos(\phi-\psi)$ [where $g_\perp = \sqrt{g_x^2+g_y^2}$, $\psi = \arctan(g_y/g_x)$], and taking into account that the integral of a periodic function over an entire period is unchanged when the limits of integration are shifted together, we can evaluate the $\phi$ and $\rho$ integrals in (B1) as follows:

$$\int_{-\pi}^{\pi} d\phi e^{-ix\cos\phi} = 2\pi J_0(x) \tag{B2}$$

$$\int dx x J_0(x) = xJ_1(x) \tag{B3}$$

(see, e.g., Refs. 33 and 34). We restrict our discussion to shapes that are symmetric also under reflection in the $x,y$ plane. In that case $\theta_{\mathbf{g}}$ is real and, for a given value of $\mathbf{g}$, we can restrict the integration in (B1) to positive values of $z$, $z \in [0, z_1]$. The contribution from negative values of $z$ is obtained by substituting $g_z \to -g_z$. Eq. (B1) then takes the form

$$\theta_{\mathbf{g}} = \frac{4\pi}{a^3 g_\perp}\int_0^{z_1} dz\rho(z)J_1[g_\perp\rho(z)]\ \cos(g_z z). \tag{B4}$$

We now discuss some specific shapes $\rho(z)$.

($a$) *Nonoverlapping cylinders.* For a cylinder of radius $R$ and height $h$ [see Fig. 8(e)] we immediately obtain

$$\theta_{\mathbf{g}} = \frac{4\pi}{a^3 g_\perp}RJ_1(Rg_\perp)\frac{\sin(|g_z|h/2)}{|g_z|}. \tag{B5}$$

($b$) *Nonoverlapping spheroids.* For a spheroid with semi-axes $b$ and $c$ [see Fig. 8(c)] the result is similar to that for a sphere

$$\theta_{\mathbf{g}} = 4\pi bc^2[\sin(\tilde{g}) - \tilde{g}\cos(\tilde{g})]/(\tilde{g}a)^3, \tag{B6}$$

where $\tilde{g} = \sqrt{c^2g_x^2 + c^2g_y^2 + b^2g_z^2}$ and where we have used the following relation:[33,34]

$$\int_0^\alpha x^2\frac{\cos(\beta\sqrt{\alpha^2-x^2})}{\sqrt{\alpha^2-x^2}}J_1(x)dx = \sqrt{\frac{\pi}{2}}\alpha^{3/2}(\beta^2+1)^{-3/4}J_{3/2}(\alpha\sqrt{\beta^2+1}). \tag{B7}$$

For $b = c = R$, (B6) reduces to Eq. (3.3)—the result for a sphere.

($c$) *Ellipsoid and other nonoverlapping shapes.* It is actually easier to obtain (B6) by viewing the spheroid as a particular type of ellipsoid. For an ellipsoid [see Fig. 8(c)] we perform the following coordinate rescaling transformation: $x \to bx', y \to cy', z \to dz'$, which transforms the ellipsoid to a sphere. Using spherical polar coordinates to evaluate $\theta_{\mathbf{g}}$ in the rescaled coordinate system, we get

$$\theta_{\mathbf{g}} = \frac{bcd}{a^3}\int_0^1 drr^2\int_0^\pi d\vartheta\cos(\vartheta)\int_0^{2\pi}d\phi \times \exp[-ibg_xx - icg_yy - idg_zz]. \tag{B8}$$

After defining $\tilde{g} \equiv \sqrt{b^2g_x^2 + c^2g_y^2 + d^2g_z^2}$, all the evaluations are similar to the spherical case. The final result is shown in Table II. The expression for $\theta_{\mathbf{g}}^{(\mathrm{sphere})}$ [see (3.3)] can be obtained from (B8) by taking $b = c = d = R$.

The case of parallelepiped-shaped inclusions could easily be handled by using affine coordinates for evaluating $\theta_{\mathbf{g}}$. In Table II [and also in Fig. 8(d)] we show results only for a rectangular prism.

Another shape for which $\theta_{\mathbf{g}}$ can be evaluated in closed form is the parabolic lens, described by $\rho(z) = \sqrt{l^2 - az}$. Substituting this profile in the integral of (B4), we obtain a closed form analytical expression for $\theta_{\mathbf{g}}$ (see Table II).

($d$) *Overlapping spheres.* This is the most difficult case that we considered [see Fig. 8(b)]. We first evaluate the Fourier integral over a sphere from which two diametrically opposed protrusions have been removed: that is the integral which appears in (3.7). For the special case $g_\perp = 0$, that integral takes the form

$$I(0,g_z,R,a) = \begin{cases} -2\pi\frac{\cos(g_z a/2)}{(g_z a)^2} & \text{for } g_z \neq 0, \\ -\pi\left[\frac{1}{12} - \left(\frac{R}{a}\right)^2\right] & \text{for } g_z = 0. \end{cases} \tag{B9}$$

This result holds for all $g_z$ of the form $g_z = \frac{2\pi}{a}n_z$, where $n_z$ is an integer. To evaluate (3.7) for an arbitrary nonzero value of $\mathbf{g}$, we need to use the series expansion of $xJ_1(x)$, which includes only even powers of $x$, and then substitute the finite binomial expansion of $x^{2m} = [g_\perp^2(R^2 - z^2)]^m$ in powers of $z^2$. In this way we get a double series expansion for the integrand of (3.7), but the remaining integrals are then elementary

$$\begin{aligned} I(g_\perp,g_z,R,a) = {} & \frac{2\pi}{a^3}\sum_{k=0}^{\infty}\frac{1}{k!}\left(-\frac{g_\perp^2R^2}{4}\right)^k \\ & \times\sum_{l=0}^{k+1}\frac{(-1)^l R^{-2l+2}}{l!(k+1-l)!}\int_0^{a/2} z^{2l} \\ & \times\cos(|g_z|z)dz. \end{aligned} \tag{B10}$$

For simplicity we consider first the case $g_z = 0$. In that case the integral in (B10) is easily evaluated and we get the following double series result:

$$\begin{aligned} I(g_\perp,0,R,a) = {} & 2\pi\left(\frac{R}{a}\right)^3\sum_{k=0}^{\infty}\frac{1}{\Gamma(1+k)}\left(-\frac{g_\perp^2R^2}{4}\right)^k \\ & \times\sum_{l=0}^{k+1}\frac{(-1)^l(a/2R)^{2l+1}}{(2l+1)\Gamma(2+k-l)\Gamma(1+l)}, \end{aligned} \tag{B11}$$

where $\Gamma(k)$ is the complete gamma function. The sum on $l$ can be extended to $\infty$ since, for $l > k+1$, the function $\Gamma(2+k-l)$ in the denominator becomes infinite. Therefore, we can perform the $k$ summation first to get

$$\begin{aligned} I(g_\perp,0,R,a) = {} & -2\pi\left(\frac{R}{a}\right)\left(\frac{1}{g_\perp a}\right) \\ & \times\sum_{l=0}^{\infty}\frac{J_{l-1}(g_\perp R)}{l!(2l+1)}\left(\xi\frac{g_\perp R}{2}\right)^l, \end{aligned} \tag{B12}$$

where $\xi = \left(\frac{a}{2R}\right)^2$. For $\xi = 1$ this series converges to (3.3). In order to prove this we use the formula

$$\sum_{l=0}^{\infty}\frac{J_{l+\nu}(x)}{(2l+1)l!}\left(\frac{x}{2}\right)^l = \sqrt{\frac{\pi}{2x}}H_{\nu-\frac{1}{2}}(x), \tag{B13}$$

where $H_\nu(x)$ is the Struve function (see Ref. 34). This also proves that the series (B12) converges for all $\xi < 1$, i.e., for all $R > a/2$.

Turning to the general case, we perform the integration in (B10) to get

$$\begin{aligned} I(g_\perp,g_z,R,a) = {} & 2\pi\left(\frac{R}{a}\right)^3\left(\frac{2}{|g_z|a}\right)\sum_{k=0}^{\infty}\frac{1}{\Gamma(1+k)} \\ & \times\left(-\frac{g_\perp^2R^2}{4}\right)^k\sum_{l=1}^{k+1}\frac{(-1)^l(2l)!}{\Gamma(2+k-l)\Gamma(1+l)} \\ & \times\left(\frac{a}{2R}\right)^{2l+1}\sum_{m=0}^{l-1}(-1)^m \\ & \times\frac{(|g_z|a/2)^{-2m-1}}{(2l-2m-1)!}\cos(|g_z|a/2). \end{aligned} \tag{B14}$$

Again, the summation on $l$ can be extended to $\infty$, and we can, therefore, perform the $k$ summation first to get

$$\begin{aligned} I(g_\perp,g_z,R,a) = {} & -\frac{\pi\cos(|g_z|a/2)}{(a|g_z|)^2}\sum_{l=0}^{\infty}\frac{\Gamma(3+2l)}{\Gamma(2+l)} \\ & \times\left(\xi\frac{g_\perp R}{2}\right)^l J_l(g_\perp R)\sum_{m=0}^{l}(-1)^m \\ & \times\frac{1}{\Gamma(2+2l-2m)}\left(\frac{2}{|g_z|a}\right)^{2m}. \end{aligned} \tag{B15}$$

The remaining summations must be performed numerically. Although the sums over $m$ converge very rapidly, the summation over $l$ has turned out to be problematic. This is due to the appearance of a ratio of gamma functions, equal to $(2l+2)!/(l+1)!$, which increases very rapidly with $l$. Consequently, we have found it preferable to change the order of summation over $l$, $m$ and to define a new function

$$\begin{aligned} f(2m;\xi,g_\perp) \equiv {} & \sum_{l=m}^{\infty}\frac{\Gamma(3+2l)}{\Gamma(2+l)\Gamma(2+2l-2m)} \\ & \times\left(\xi\frac{g_\perp R}{2}\right)^l J_l(g_\perp R), \end{aligned} \tag{B16}$$

so as to finally get

$$\begin{aligned} I(g_\perp,g_z,R,a) = {} & -\pi\cos(|g_z|a/2)\left(\frac{1}{a|g_z|}\right)^2 \\ & \times\sum_{m=0}^{\infty}(-1)^m f(2m;\xi,g_\perp)\left(\frac{2}{|g_z|a}\right)^{2m} \end{aligned} \tag{B17}$$

The function $f(2m;\xi,g_\perp)$ was first evaluated numerically and its values were then used in (B17). In spite of the fact that the values of $f(2m;\xi,g_\perp)$ increase with $m$, when they were used in (B17) the sum always converged rapidly to a finite value.

---

[1] E. Yablonovich, T.J. Gmitter, and K.M. Leung, Phys. Rev. Lett. **67**, 2295 (1991).

[2] D.J. Bergman and Y.M. Strelniker, Phys. Rev. B **49**, 16 256 (1994).

[3] I. Webman, J. Jortner, and M.H. Cohen, Phys. Rev. B **15**, 1936 (1977).

[4] B.I. Shklovskii, Zh. Eksp. Teor. Fiz. **72**, 288 (1977) [Sov. Phys. JETP **45**, 152 (1977)].

[5] J.P. Straley, J. Phys. C **13**, 4335 (1980).

[6] J.P. Straley, J. Phys. C **13**, L773 (1980).

[7] D.J. Bergman, *Percolation Structures and Processes*, edited by G. Deutscher, R. Zallen, and J. Adler, Annals of the Israel Physical Society Vol. 5 (Adam-Hilger, London, 1983), pp. 297–321.

[8] D.J. Bergman, E. Duering, and M. Murat, J. Stat. Phys. **58**, 1 (1990); still more references can be found in this article.

[9] D.J. Bergman and D. Stroud, Phys. Rev. B **32**, 6097 (1985).

[10] A.S. Skal, Dokl. Akad. Nauk SSSR **260**, 602 (1981) [Sov. Phys. Dokl. **26**, 872 (1981)].

[11] A.S. Skal, J. Phys. C **18**, 3483 (1985).

[12] A.S. Skal, J. Phys. C **20**, 245 (1987).

[13] D.J. Bergman, Philos. Mag. B **56**, 983 (1987).

[14] D.J. Bergman, Y. Kantor, D. Stroud, and I. Webman, Phys. Rev. Lett. **50**, 1512 (1983).

[15] U. Dai, A. Palevski, and G. Deutscher, Phys. Rev. B **36**, 790 (1987).

[16] M. Rhode and H. Micklitz, Phys. Rev. B **36**, 7289 (1987).

[17] D. Stroud and D.J. Bergman, Phys. Rev. B **30**, 447 (1984).

[18] A.M. Dykhne, Zh. Eksp. Teor. Fiz. **59**, 641 (1970) [Sov. Phys. JETP **32**, 348 (1971)].

[19] K.S. Mendelson, J. Appl. Phys. **46**, 4740 (1975).

[20] C. Herring, J. Appl. Phys. **31**, 1939 (1960).

[21] H. Stachowiak, Physica **45**, 481 (1970).

[22] D. Stroud, Phys. Rev. B **12**, 3368 (1975).

[23] D. Stroud and F.P. Pan, Phys. Rev. B **13**, 1434 (1976).

[24] J.B. Sampsell and J.C. Garland, Phys. Rev. B **13**, 583 (1976).

[25] B.Ya. Balagurov, Fiz. Tverd. Tela **28**, 3012 (1986) [Sov. Phys. Solid State **28**, 1694 (1986)].

[26] L.N. Gorodzha and Yu.P. Emets, Zh. Tekh. Fiz. **52**, 1705 (1982) [Sov. Phys. Tech. Phys. **27**, 1047 (1982)].

[27] A.K. Sarychev, D.J. Bergman, and Y.M. Strelniker, Europhys. Lett. **21**, 851 (1993).

[28] A.K. Sarychev, D.J. Bergman, and Y.M. Strelniker, Phys. Rev. B **48**, 3145 (1993).

[29] D.J. Bergman and K.J. Dunn, Phys. Rev. B **45**, 13 262 (1992).

[30] G.A. Baker, Jr., *Essentials of Padé Approximants* (Academic Press, New York, 1975).

[31] G.A. Baker, Jr. and P.R. Graves-Morris, *Encyclopedia of Mathematics and its Applications*, edited by G.C. Rota (Cambridge University Press, London, 1981), Vol. 14, Pts. I and II.

[32] D.J. Bergman and Y.M. Strelniker (unpublished).

[33] I.S. Gradshteyn and I.M. Ryzhik, *Table of Integrals, Series and Products* (Academic Press, New York, 1965).

[34] A.P. Prudnikov, Yu.A. Brychkov, and O.I. Marichev, *Integrals and Series*, Vols. 1–3 (Gordon and Breach Science Publishers, New York, 1986).

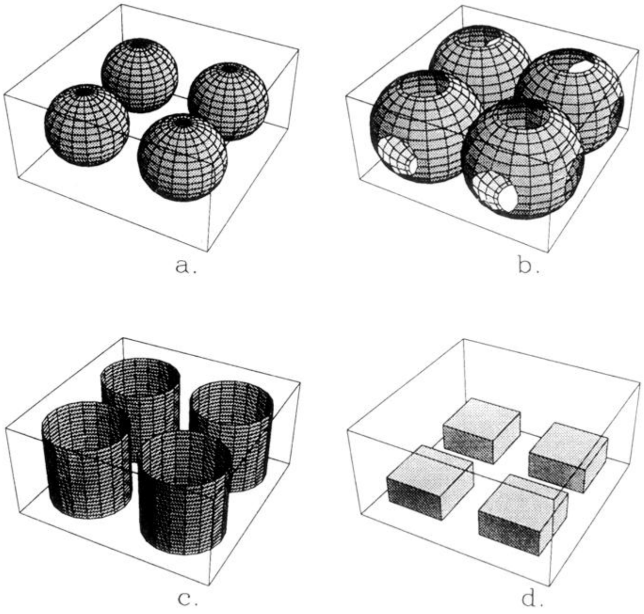

FIG. 1. Possible examples of a periodic composite microstructure with various shapes of inclusions: (a) Nonoverlapping spheres, (b) overlapping spheres, (c) nonoverlapping cylinders, (d) nonoverlapping rectangular prisms.